Levulinic to succinic acid transformation over Ru based catalysts

Luis Alejandro Arriaga-Arellano, Débora Álvarez-Hernández, María Isabel Domínguez, Marcela Martínez T., Anna Penkova, Svetlana Ivanova, Miguel Ángel Centeno [*]

Departamento de Química Inorgánica e Instituto de Ciencia de Materiales de Sevilla, Centro mixto CSIC-Universidad de Sevilla, 41092 Sevilla, Spain

ARTICLE INFO

ABSTRACT

In this work ruthenium based catalysts are tested as catalytic systems for the selective oxidation of levulinic to succinic acid. Very different in nature supports have been chosen in order to elucidate the effect of their textural and acidic properties on the final catalytic activity. The influence of Ru particle size is also discussed and proposed as one of the key factors. Medium range ruthenium particles supported on relatively acid supports are the best performing systems in terms of succinic acid yield, while the most active catalysts in terms of conversion result in important carbon loss due to reagent/products full oxidation.

Introduction

Nowadays, the oil refining industry produces practically all commodities essential for the human activity, enabling a rapid development of the world economy. However, this hydrocarbon economy is also environmentally unsustainable in long terms and needs to be replaced by a renewable and more friendly carbohydrate (biomass) economy in line with the Triple Bottom Line concept, which implies the use of processes that combine ecological integrity, social responsibility and economic viability [1]. Theoretically, almost all petroleum-derived chemicals can be obtained by biorefining. To a large extent, it will be the price differences between their respective feedstocks that will determine whether these chemicals must be produced from biomass or from petroleum [2]. As a consequence, the biorefinery of the future is expected to be based on a limited number of cost-effective platforms [3].

Biomass is considered especially important for the transformation of molecules with relatively high oxygen content in other functionalized value-added molecules such as hydroxymethylfurfural (HMF) or levulinic acid (LA) and products derived from it: 1,4-pentanediol, γ-valerolactone or succinic acid (SA) among others [4–6]. Indeed, LA appears to be the best starting molecule to obtain succinic acid (SA), a chemical product that can be found in the top 10 value added chemicals issued from biomass with an increasing market value of around 400 billion USD per year [4,7,8]. SA is used in the production of food additives, biodegradable polymers, detergents, etc. and also as platform molecule to produce other high value chemical products such as tetrahydrofuran, γ-butyrolactone, maleic anhydride, etc. [9–12]. Currently the

technologies available for the production of succinic acid rely on both, fossil fuels (mainly by butane oxidation using maleic anhydride to SA) or biological means (biomass fermentation process using bacteria or yeasts), the latter suffering limitations such as difficult pH control, separation and enzyme deactivation [13–15]. Still from economic point of view, the petrochemical route is slightly more viable than the biological one (2.40–2.60 $/kg vs. 2.86–3.00 $/kg) [16,17]. In the last years as an alternative to the usual ways for SA production, the oxidation of furfural [18] or levulinic acid either referring to Baeyer-Villiger oxidation with hydrogen peroxide [4,12,19] or oxidation with molecular oxygen [20] have been reported as biorefinery routes. The very first report on LA to SA transformation dates from 1879 but it is in the last decade with the discovery of SA current significance in green chemistry that some more reports appear about the oxidation of levulinic acid or its alkyl esters. The application of Mn (III) as a catalyst in the oxidation of methyl levulinate under 5 O_2 bar and 90 °C, reported as mild conditions, has been published, but the low selectivity to SA did not allow yields superior to 52% after 20 h of reaction [21]. The use of a V_2O_5-based catalyst in the oxidation of LA to SA with O_2 at temperatures between 365 and 400 °C leaded to 81% of SA yield [22], requiring hard pressure conditions. Bromoamides in perchloric acid ($HClO_4$) (oxidizing agent), mercuric acetate [$Hg(OAc)_2$] and $RuCl_3$ as catalyst have been also reported for the LA transformation to SA. Nevertheless, the use of mercuric acetate classifies this process as harmful for environment [23]. The effect of the solvent and starting substrate (levulinic acid or methyl levulinate) over succinic acid yield has been studied over manganese acetate [24]. Ru-based catalysts have appeared as very good candidates

---

for levulinic acid oxidation. Podolean et al. [20] have studied a ruthenium catalyst supported on magnetic nanoparticles coated with SiO_2 and functionalised with (3-aminopropyl) triethoxysilane. Different reaction conditions like pressure (5–14 bar O_2), temperature (100–180 °C) time (6–10 h), and different solvents (acetone, methanol, ethanol, water, etc.) have been optimized in order to achieve optimal SA production (79% of conversion of LA and 98,6% selectivity to SA). A great diversity of catalysts appears when using H_2O_2 as oxidant, such as H_2WO_4 [4], trifluoroacetic acid [12] or in-situ generated t-BuOI [19], Amberlyst-15 [25].

Considering that the key aspect to find a way for succinic acid production is to use benign oxidation sources and appropriate heterogeneous catalysts (easily recoverable after the reaction for reuse) that favors mild conditions and shows a good activity/selectivity balance this work devotes to the screening of Ru-based nanoparticles supported on various commercial supports with the objectives of achieving easy to prepare, cheap and environmentally friendly heterogeneous catalysts and identifying how the support affects succinic acid yield. The catalysts performance over the same catalysts in presence of oxygen and hydrogen peroxide is contrasted and discussed in details.

Experimental

Synthesis of the Ru based catalysts

The catalysts were prepared using wet impregnation of the metallic precursor, ruthenium nitrosyl nitrate ($RuNO(NO_3)_3$, 14.32%, Johnson Matthey) over six different supports: iron (III) oxide (Fe_2O_3, 99%, Merck), cerium (IV) oxide (CeO_2, 99.995%) Sigma-Aldrich, alumina (Al_2O_3, Sasol), silica (SiO_2, Evonik Industries), ammonium mordenite ($SiO_2/Al_2O_3 = 20$, Zeolyst) and activated charcoal (DARCO, 100 mesh particle size, Sigma-Aldrich).

In a typical preparation (3 g total, 5% w/w of Ru), a corresponding amount of each support (Fe_2O_3, CeO_2, Al_2O_3, SiO_2 and zeolite (stands for mordenite)) is added to 100 mL of an aqueous solution of 1.0475 g $RuNO(NO_3)_3$. After mixing the excess of solvent was evaporated using a rotary evaporator (BUCHI, R-215) in the following procedure: (i): 15 min stirring (175 rpm) at room temperature (RT), (ii) 15 min of stirring (175 rpm) at reduced pressure (70 mbar) at RT and (iii) evaporation at the same stirring and vacuum conditions at 50 °C for 1 h approximately. The obtained solids were dried 24 h at 80 °C and milled in agate mortar. All samples were calcined in oven under static air atmosphere for 2 h at 400 °C at a heating rate of 10 °C.min^{-1} and reduced for 2 h under H_2:N_2 (1:1, 100 mL min^{-1}) at 250 °C (10°.min^{-1} heating rate) to obtain the final catalysts: Ru/Fe_2O_3, Ru/CeO_2, Ru/Al_2O_3, Ru/SiO_2 and Ru/Zeo.

As for the Ru/C catalyst, the synthesis process was similar, but the used solvent and thermal treatment were slightly different. The wet impregnation was carried out in acetone with evaporation at 556 mbar and 40 °C. Due to the carbon loss that can occur during the oxidation step only a reduction pretreatment was carried out in the conditions described above.

Characterization techniques

X-ray diffraction was used to obtain information about the crystalline structure and crystallite domain size of the prepared solids. X'Pert Pro diffractometer equipped with a Cu anode (Cu-Kα 40 mA, 45 kV) was used for the measurements, setting a step size of 0,05° and an acquisition time of 300 s in the 10–90°2θ range. The crystalline structure was determined using PDF2 ICDD2000 (Powder Diffraction File 2, International Center for Diffraction Data, year 2000) database, and the crystallite size was determined using Scherrer equation:

$$L = \frac{K\lambda}{\beta Cos2\theta} \tag{1}$$

where K is a non-dimensional shape factor (0,9 in this case), λ is the wavelength of the Cu anode (1.54 Å, Kα), β is the full width at half maximum (FWHM) of the analyzed peak and 2θ represents its position.

For the carbonaceous materials, the L_a and L_c parameters (crystallite dimension along the a and c axis) were calculated according to Rodríguez et al. [26].

A dispersive microscope Horiba Jobin Yvon LabRam (HR800) equipped with a CCD detector and a green He-Ne laser ($\lambda = 532,14$ nm and P = 5 mW) was used to carry out the Raman measurements. The used laser spot size was of 0,72 μm (360 nm of spatial resolution), obtained by using a 50X objective lens, grating of 600 grooves per mm and a confocal aperture of 1.000 μm.

Brunauer–Emmett–Teller method (BET) was used to calculate the specific surface area, after nitrogen adsorption isotherm measurements at 77 K in a TriStar II 3020 automated gas adsorption analyzer. Prior analysis, all samples were degassed in vacuum at 250 ºC during 2 h, exception made by Ru/Zeo and Ru/C, which were treated at the same temperature during 24 h.

The transmission electron microscopy (TEM) images were used to confirm the presence of Ru nanoparticles and their distribution on the supports. The images were obtained in a PHILIPS CM-200 TEM, equipped with a EDX microanalysis. The minimal spot size was 15 nm with maximum resolution of 2,8 Å.

X-ray photoelectron spectroscopy (XPS) was used to determine the chemical composition of samples' surface. SPECS photoelectron spectrometer equipped with an PHOIBOS 150 MCD analyzer, working at 40 eV constant step energy and 1,0 eV resolution was used in ultra-high vacuum of 10^{-10} mbar with X-ray source with Kα emission originated on aluminum target with energy of 1.486 eV, 0,85 eV band width, 250 W power and 12,5 kV constant potential. The XPS spectra were recorded at room temperature and the bond energy was calibrated over C1s adventitious at 284,6 eV with an uncertainty of $\pm 0,2$ eV. Spectra treatments were carried out using Casa XPS program. Spectra deconvolution was performed using a Shirley baseline and Lorentzian-Gaussian peak shape and the relative Sensitivity Factors (RSF) was used for quantification purposes directly from Casa Software.

The temperature-programmed desorption of ammonia (NH_3-TPD) was used to provide information about the type and strength of the acid sites in the samples. For the measurements a quartz reactor equipped with 50 mg of 100–200 μm sieved catalyst was used. Prior NH_3 adsorption in 100 mL.min^{-1} of 5:95 NH_3:He mixture at 50 °C during 1 h, the samples were pre-treated at 200 °C during 1 h in 100 mL.min^{-1} of He to eliminate any adsorbed water. After that, the physisorbed NH_3 was eliminated at 50 °C during 1 h in a pure He flow, and the temperature allowed to increase from 50° to 600°C with a heating rate of 5 °C.min^{-1} to register chemisorbed NH_3 desorption. Gas outlet was monitored by mass spectrometry in a Pfeiffer Vacuum Prisma Plus equipment. 17 and 18 m/z signals were measured, and ammonia evolution considered as the one at $m/z = 17$ after subtraction of the water contribution to this signal (considered as 26% of $m/z = 18$).

Catalytic activity

Levulinic acid oxidation using O_2

The levulinic acid (LA) oxidation was carried out in a batch pressure reactor of 50 mL (PARR, model 4597), equipped with temperature, magnetic stirring and pressure controllers. In a typical reaction, an aqueous solution of levulinic acid (LA) (0,05 M, 10 mL) and 50 mg (0,0025 mmol Ru) reduced Ru catalysts were mixed in a Teflon liner, that is placed into the reactor. After closure, a purge with 10 bar of O_2 was carried out. Then, the reactor was pressurized with O_2 at 20 bar at room temperature and the stirring rate of 400 rpm and 10 °C.min^{-1} heating rate were set to reach the reaction temperature of 150 °C, at which the reaction took place during 6 h. After this, the reaction was stopped, by turning off the heating and immersing the reactor in an ice-cold water bath, keeping the stirring to cool down the system as quick as
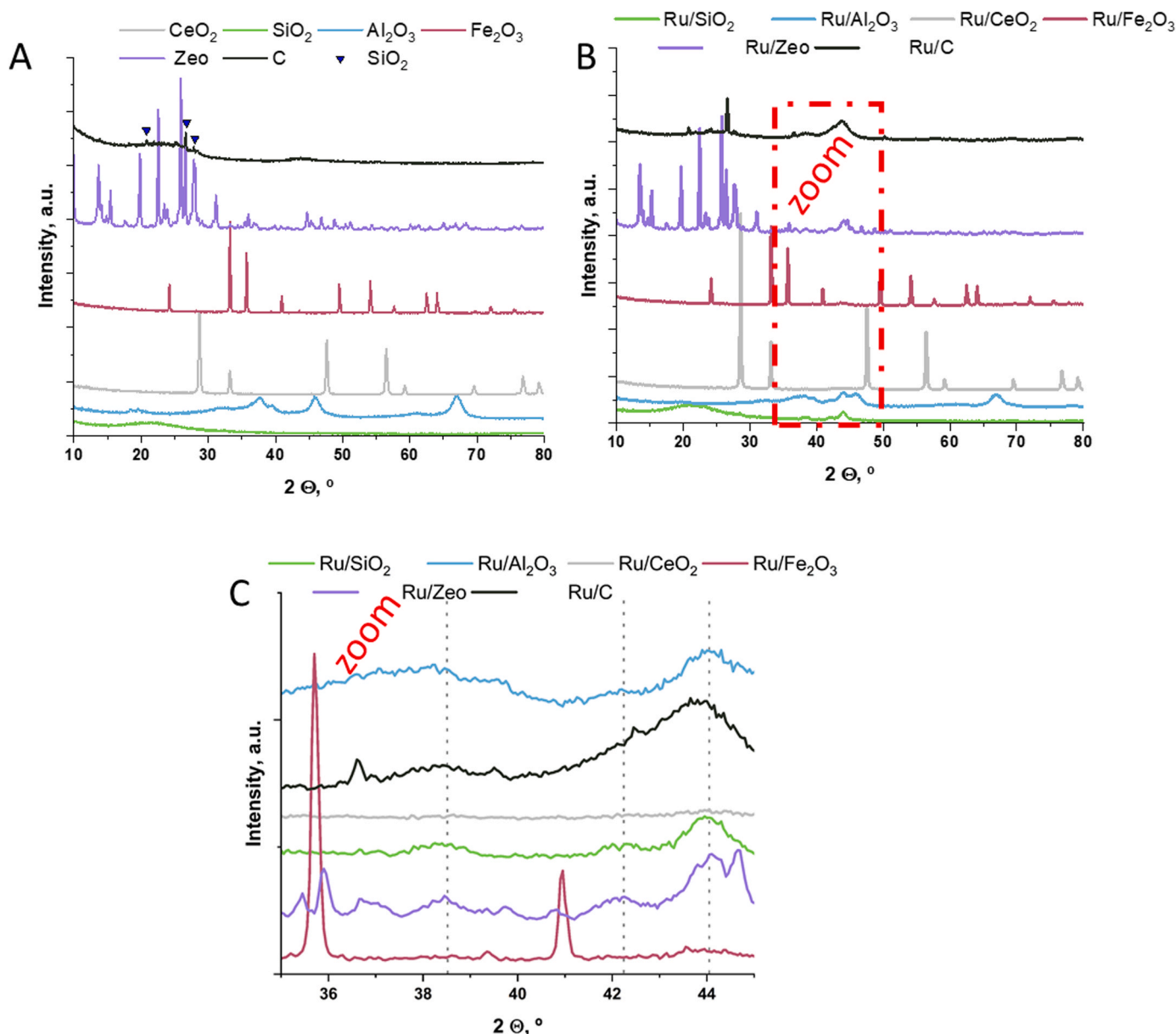
Fig. 1. X-ray diffraction patterns of the A) supports and B) corresponding catalysts, C) zoom of the Ru main diffraction window 35–45 ° 2 Θ.

possible to RT. Then, the reactor was depressurized, and the reaction mixture was microfiltered, diluted and analyzed using an HPLC chromatograph (Agilent 1260 Infinity ll), equipped with Agilent Hi-Plex H column, a RI G7162A detector and using as mobile phase 0005 M H_2SO_4 solution in milli-Q water.

Levulinic acid oxidation using H_2O_2

Levulinic acid oxidation with H_2O_2 have been carried out in Syrris automated flow batch system allowing six reactions in the same conditions of stirring, temperature and atmosphere. In a typical reaction an aqueous solution of levulinic acid (LA) (0,05 M, 10 mL) and 50 mg (0,0025 mmol Ru) of catalysts are mixed with 3 equivalents of H_2O_2. The temperature was raised to 90ºC for the desired time and the products of the reaction microfiltered and analyzed in HPLC.

Products yield, levulinic acid conversion, and turnover number (TON) were calculated according the following equations:

$$Yield \quad (\%) = \frac{n_P}{n_{LA}^o} * 100 \tag{2}$$

$$Conversion \quad (\%) = \frac{n_{LA}^o - n_{LA}^f}{n_{LA}^o} * 100 \tag{3}$$

$$TON = \frac{n_P}{n_{Ru} * D}$$

where n_P is the number of moles of the product p, n_{LA}^o are the initial moles of levulinic acid, n_{LA}^f are the final moles of levulinic acid, n_{Ru} are the moles of ruthenium, and D the particle dispersion estimated from the average particle size measured by TEM and mathematical model of cuboctahedral particles [27].

The carbon balance was also calculated, as the recovered C after the reaction

$$Carbon \quad balance \quad (\%) = \frac{n_C^f}{n_C^o} * 100$$

where n_C^o are the initial moles of C and n_C^f are the final moles of C detected within the products and non-converted reagent.

Table 1

Crystallite size before and after thermal treatments of the supports and active phase, calculated by XRD or measured by TEM, and metal dispersion.

Catalyst	Crystallite size (nm)					Dispersion (%)
	Ru, XRD	Support			Ru, TEM	
	Ru	Initial	Final	Ru	Ru	Ru
Ru/C	*n.c.*	3.6/3 (L_a/L_c)	2.6/2.4 (L_a/L_c)	2.2 ± 0.4		55
Ru/Zeo	10.7	89.1	122.7	9.3 ± 2.4		15
Ru/SiO$_2$	9	1.2	1.2	8.1 ± 1.9		17
Ru/CeO$_2$	6.8	51.5	179	8.5 ± 2.0		16
Ru/Fe$_2$O$_3$	5.7	218.7	360.4	4.2 ± 1.2		31
Ru/Al$_2$O$_3$	5.9	6.1	5.7	11.5 ± 3.5		13

n.c. not calculated.

Results and discussion

The diffraction patterns of the parent supports are presented in Fig. 1A. The corresponding phases are identified: mordenite (#00–043–0171), SiO$_2$ (#00–027–0605), CeO$_2$ (#00–034–0394), Fe$_2$O$_3$ (#01–072–0469) and Al$_2$O$_3$ (#00–029–0063). The crystallinity of the supports is very different with mordenite, CeO$_2$ and Fe$_2$O$_3$ very crystalline solids and Al$_2$O$_3$, SiO$_2$ and carbon poorly crystalline. The carbon support presents the wide characteristic diffractions of the amorphous carbons at 2θ ≈ 25° and 44°, associated with (002) and (100) diffraction planes, respectively. In addition, the appearing of some intense diffractions for the carbon sample indicates the presence of quartz (#01–085–1054) impurities, commonly found in DARCO commercial carbon.

In the diffraction patterns of the catalysts (Fig. 1B and zoom in Fig. 1C), the supports diffractions pertain together with those of metallic Ru (# 00–006–0663). For the Ru/C sample, the diffractions associated with Ru are superposed with the carbon diffractions making difficult the estimation of metallic particle size. Nevertheless, the changes in this zone in comparison to the parent support clearly indicate the presence of well dispersed Ru particles (Fig. 1C).

Table 1 shows the crystallite sizes for Ru^0 and corresponding supports estimated from Scherrer equation. All catalysts (excepting Ru/C) present Ru^0 sizes ranging from 6 to 11 nm. A closer sight allows the differentiation of two groups of solids, Ru/zeolite and Ru/SiO$_2$, with Ru particles around 9–11 nm, and Ru/Al$_2$O$_3$, Ru/Fe$_2$O$_3$ and Ru/CeO$_2$ with smaller particles around 5–7 nm.

Regarding the supports, the results suggest that the crystallite size of the SiO$_2$ and the Al$_2$O$_3$ does not change considerably after Ru deposition in respect to the bare support. Same for the carbon crystallite parameters: L_a and L_c, the Ru impregnation and thermal treatments do not cause significant changes. However, for the zeolite, CeO$_2$ and Fe$_2$O$_3$, the crystallite size increase after the reduction treatment.

A noticeable increase in crystallite size for CeO$_2$ after the thermal treatments is also confirmed by Raman spectroscopy (Fig. 2A). A shift of the main CeO$_2$ band from 464 to 460 cm^{-1} and a decrease of FWHM (full width at half maximum) from 34 to 17 cm^{-1} is observed indicating an increase in symmetry associated with the increase of crystalline size domain. Usually, the bands at 460 cm^{-1} and 604 cm^{-1} are associated with CeO$_2$ and its defects [28] and the ratio of its intensities (I_{460}/I_{604}) is a parameter that allows the estimation of oxygen vacancies present in the structure [29]. The lower the ratio I_{460}/I_{604} the higher the vacancies population within the ceria structure. Considering this and the fact that the I_{460}/I_{604} value for Ru/CeO$_2$ is higher than the one for pure CeO$_2$, we can suggest vacancies reduction for the Ru/CeO$_2$ and increase in crystallinity in agreement with the XRD analysis.

In addition to the mentioned crystalline structure changes, the presence of a band at ≈ 190 cm^{-1} in the Ru/CeO$_2$ and its absence for the bare support, is an indicator of the presence of Ru^0 in the CeO$_2$ support [30]. Also, the decrease in the intensity of the bands associated with peroxides and superoxides at 975, 1073, 1177 and 1359 cm^{-1} in the Ru/CeO$_2$ [18] in comparison to CeO$_2$ support's bands, suggests a decrease in the quantity of these species, also associated to lower exposed surface.

The Raman spectrum of the Ru/C catalyst (Fig. S1) presents the characteristics bands of carbonaceous solids in (i) the first order zone (1000–1800 cm^{-1}) and (ii) in the second order zone (2500–3400 cm^{-1}) [26]. The two bands at 1580 cm^{-1} and 1350 cm^{-1} are very characteristic for carbon based materials. The band at 1580 cm^{-1}, known as G band or graphite band is associated with the vibration mode of graphite (sp^2 hybridized) carbon with E$_{2g}$ symmetry and it is related to the degree of graphitization of the solid, while the band at 1350 cm^{-1}, known as D band or defects band, is related with the existence of defects and partial disorder in the sp^3 carbon structure and the presence of sp^3 hybridized carbon [26]. In the second order zone, three bands at 2598, 2898 y 3171 cm^{-1} represent the respective overtone (2D=2680cm^{-1} y 2 G = 3200 cm^{-1}) and combination bands (D+G=2940 cm^{-1}) of the main D and G bands. On the other hand, no bands associated with Ru^0 are detected for this catalyst, contrary to all other samples, where the characteristic Ru^0 band at 189 cm^{-1} appears (Fig. 2B).

TEM analysis of the catalysts is presented on Fig. 3.

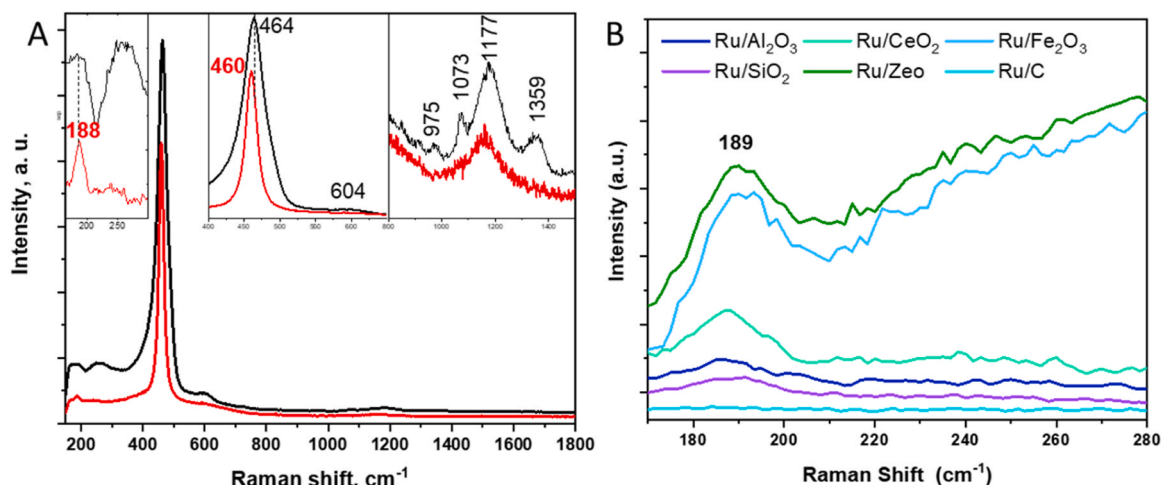After XRD and TEM analysis we can conclude that a different

Fig. 2. Raman spectra for A) CeO$_2$ vs. Ru/CeO$_2$ (in red) and B) all catalysts (zone 180–280 cm^{-1}).
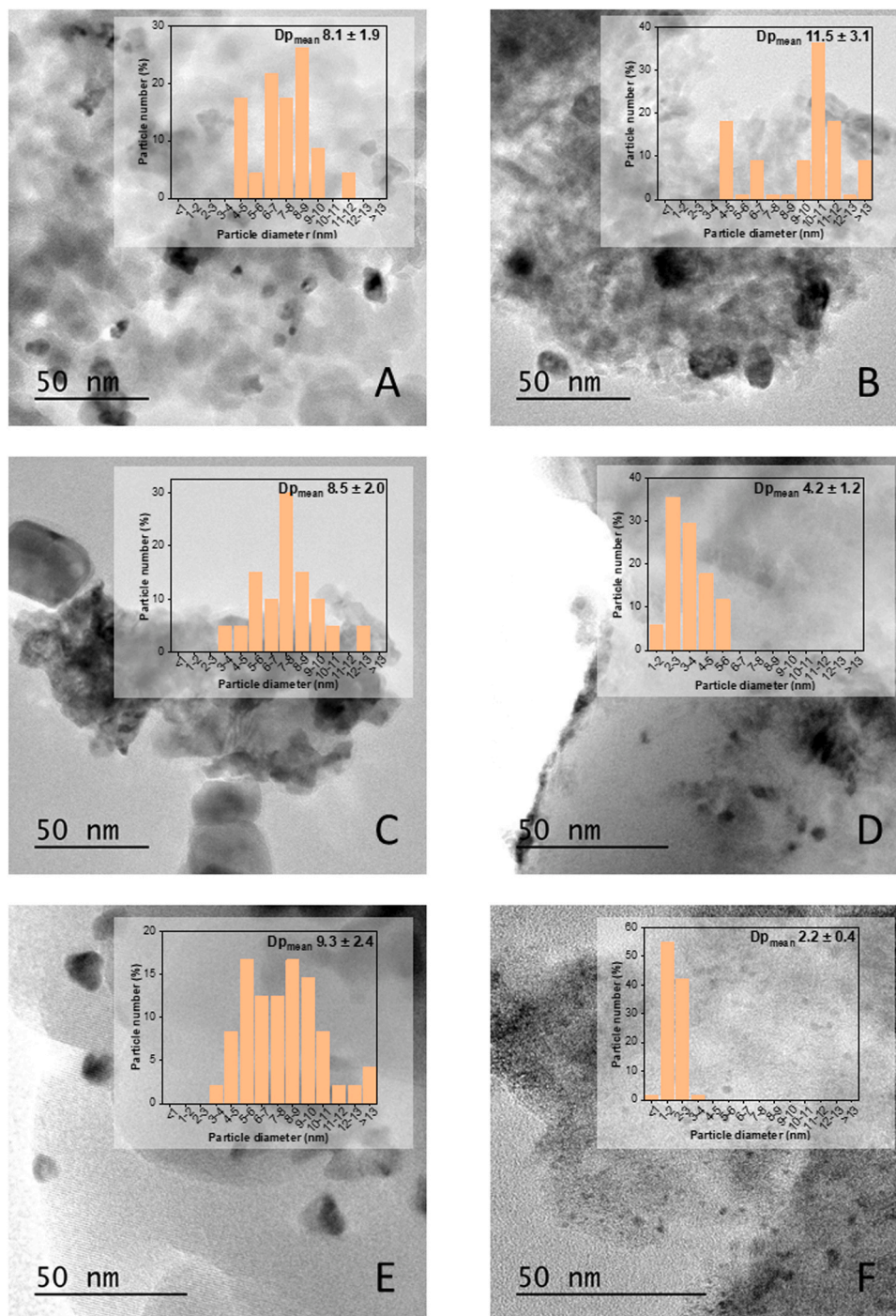
Fig. 3. TEM images and particle size distribution of A) Ru/SiO$_2$, B) Ru/Al$_2$O$_3$, C) Ru/CeO$_2$, D) Ru/Fe$_2$O$_3$, E) Ru/Zeo, F) Ru/C.

particles size distribution is found for all samples, being the Ru/C the sample with smallest Ru particle size of 2,2 nm (Table 1). The particle size of all other samples oscillates between 4 and 11 nm with mono-modal distribution of sizes in the majority of the cases, exception made by Ru/Al$_2$O$_3$ samples where particles aggregates have been observed and considered as one particle. The standard deviation increase with the increase in average size and particles agglomerates.

As for the textural characteristics the catalysts present very different properties due to the nature of the used support. Ru/C and Ru/Zeo have a very important microporous character (54% and 89% microporosity, respectively) confirmed also by the higher quantity of adsorbed gas at very low relative pressure (N$_2$ adsorption/desorption isotherms in

Fig. S2). These solids show the highest BET specific surface area (Table 2) followed by Ru/SiO$_2$ and Ru/Al$_2$O$_3$ with intermediates values (around 190 m^2/g) and Ru/CeO$_2$ and Ru/Fe$_2$O$_3$ with very low surface.

The acid properties of the catalysts are evaluated by NH$_3$-TPD. The Fig. 4 and Table 2 summarizes NH$_3$ desorption signals and corresponding calculated total area. In general, higher the temperature at which the NH$_3$ is desorbed, higher the acid force of the adsorbing site. Therefore, the signals at lower temperatures represent weaker acid sites while those at higher temperature are the stronger ones. Ru/Zeo, Ru/SiO$_2$, Ru/C and Ru/Al$_2$O$_3$ showed three signals, two superposed desorption in the lower to medium range temperatures and another at higher temperatures indicating the presence of three types of acid sites

Table 2
BET surface, pore volume and percentage of microporosity of the catalysts and total acidity.

Catalyst	BET surface area (m²/g)	Pore volume (cm³/g)	Microporosity (%)	Total area TPD NH₃ (a.u)*10⁻¹¹
Ru/Fe₂O₃	4	0,01	25	
Ru/CeO₂	7	0,03	14	
Ru/Al₂O₃	185	0,46	2	3,2
Ru/SiO₂	190	0,97	10	17,8
Ru/Zeo	437	0,08	89	179,7
Ru/C	717	0,39	54	7,5
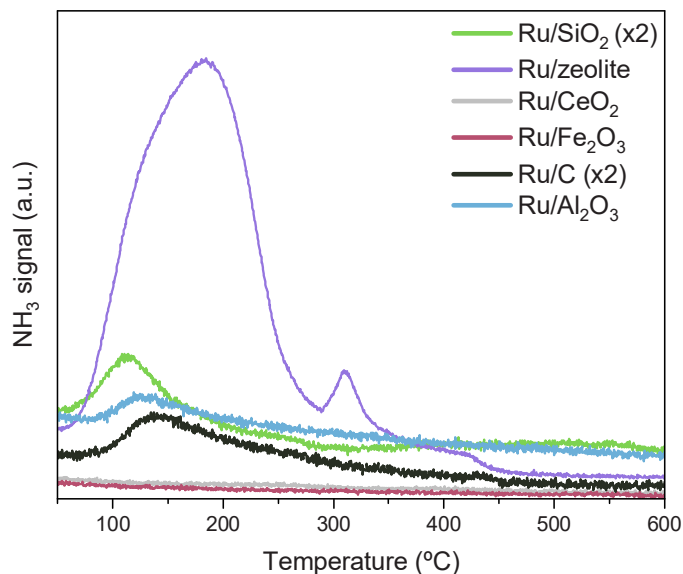
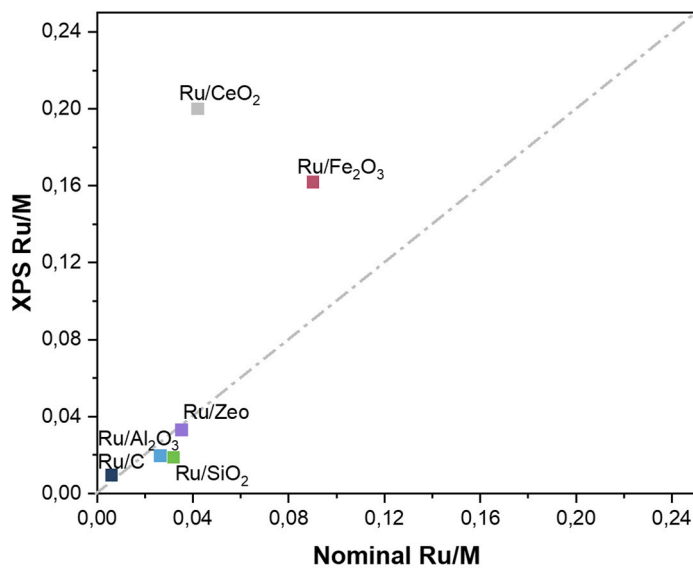**Fig. 4.** NH₃ desorption profiles of A) Ru/SiO₂, B) Ru/Al₂O₃, C) Ru/CeO₂, D) Ru/Fe₂O₃, E) Ru/Zeo, F) Ru/C.
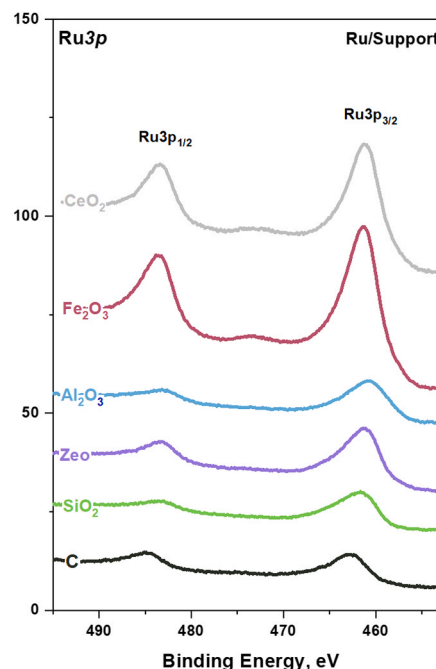
of different strength. Ru/CeO₂ and Ru/Fe₂O₃ do not show the same behavior, a negligible NH₃ desorption is detected for both samples only in the medium to high temperature range. On the other hand, the integrated area under the signals is proportional to the quantity of acid sites for a given quantity of sample (always the same 50 mg). Clearly the silica containing materials (Ru/Zeo or Ru/SiO₂) present the highest density of acid sites followed by Ru/C and Ru/Al₂O₃. The catalyst supported on zeolite presents 10–60 times higher population of low to medium strength acid sites than all the other solids.

XPS survey spectra of the catalysts are listed in Fig. S3 showing the presence of all expected elements, ruthenium and those corresponding to the support. For all samples only metallic Ru is detected in 3d (superposed with C1 s) and 3p region (Fig. 5B). The deconvolution of the C1s+Ru3d spectra has been included in the Supporting Information (Fig. S4) for all catalysts exception made by Ru/C, where the deconvolution is not reliable since carbon found in large quantities. However, the doublet recorded in the Ru3p region indicates metallic ruthenium presence on the surface. Given the difficulty of correctly quantifying Ru in the 3d zone (overlaps with C1s), the Ru3p zone were also checked. For the deconvoluted samples (all except Ru/C) the Ru3d$_{5/2}$ peak appears at 280 ± 0.2 eV, which corresponds to metallic ruthenium. Likewise, the values recorded for Ru $3p_{3/2}$ at 461 ± 0.5 eV confirm the presence of reduced Ru, being the observed minimal shift in eV between the samples originated from the different Ru-M interactions for each support [31, 32]. In any case, oxidized ruthenium is detected at higher values than indicated above [32].

The calculated surface Ru/M atomic ratio compared to the nominal one (with M being the content of the most abundant metallic element in the support) are represented in Fig. 5A. The full surface composition can be found in the Supporting Information (Table S1). The surface content of ruthenium reasonably matches the targeted one except for Ru/CeO₂ and Ru/Fe₂O₃ samples, where a very high surface concentration is determined, most probably due to the low available surface of the support. The signal intensity for Ru/CeO₂ and Ru/Fe₂O₃ confirms the high Ru presence on the surface. For those catalysts a satellite of Ru3p$_{3/2}$ appears at 472 eV, being this value similar to that of reduced ruthenium [32] as oxidized species is usually detected at lower energy around 465 eV. Based on the cross-check between Ru3d and Ru3p signals we can conclude that metallic Ru is present as prevalent initial state in all
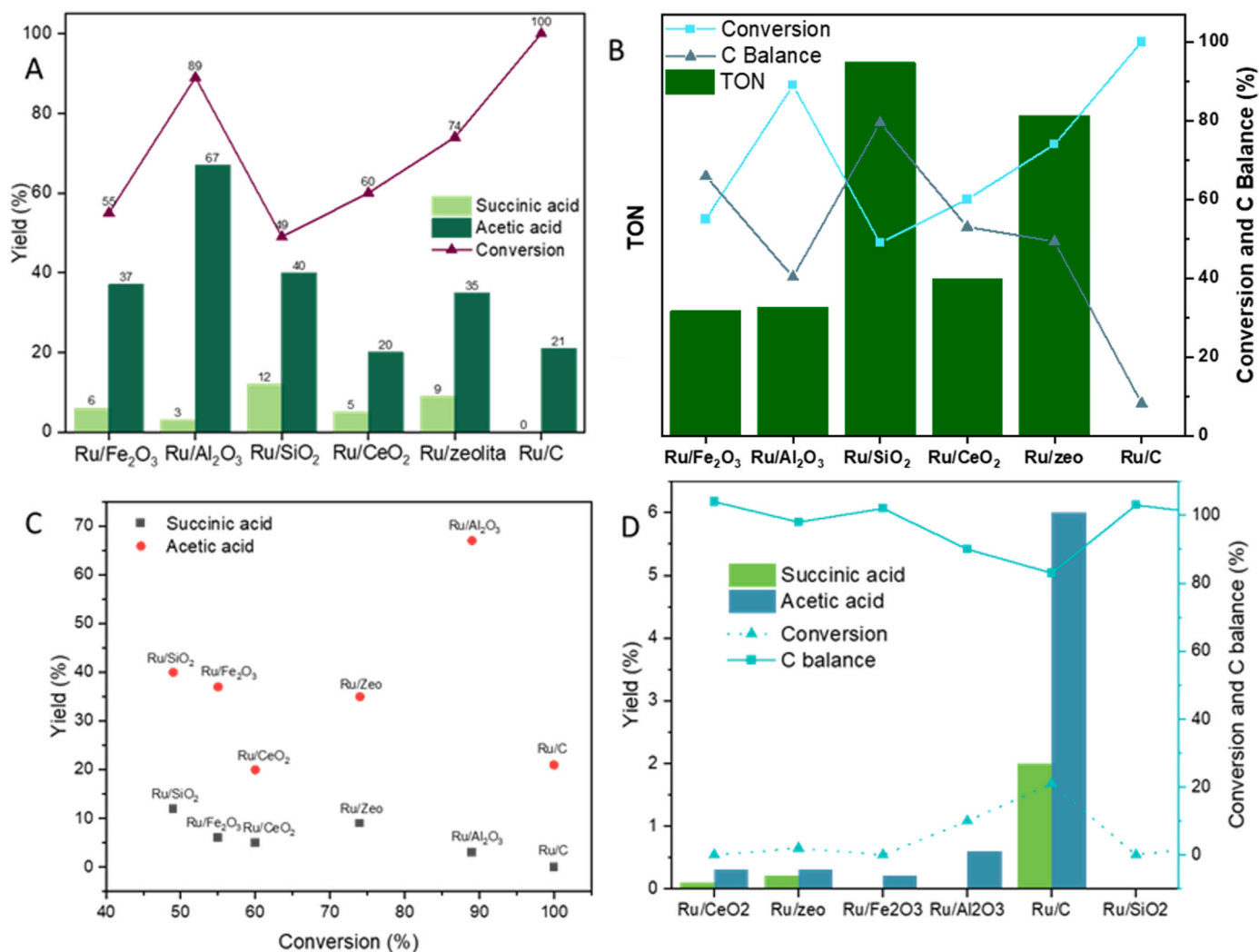

Fig. 5. A) Nominal vs. XPS surface Ru/M ratio for the studied solids, B) Ru3p for all solids.

Fig. 6. A) Succinic and acetic acid yields and levulinic acid conversion of the tested catalysts using O_2 as oxidant; B) TON, carbon balance, and conversion plot; C) yield vs. conversion plot; D) Succinic and acetic acid yields and levulinic acid conversion of the tested catalysts using H_2O_2 as oxidant.

catalysts.

The O*1 s* for some samples shows the contribution of hydroxyls and carbonates (especially for Ru/CeO$_2$ and Ru/Fe$_2$O$_3$) in addition to always present signal of O^{2-} (Fig. S5). The shift of the O^{2-} contribution is assigned to the distinct nature of M-O bonds for the different oxides.

Catalytic screening

Fig. 6A shows the levulinic acid conversion and succinic (SA) and acetic acid (AA) yields obtained for all catalysts. Both, SA and AA are the sole products of reaction in liquid phase as only non-reacted levulinic acid accompanies them in the post reaction mixture. The highest succinic acid yield (12% and 9%) is achieved by Ru/SiO$_2$ and Ru/Zeo, followed by Ru/Fe$_2$O$_3$, Ru/CeO$_2$ and Ru/Al$_2$O$_3$. Ru/C catalyst did not result in SA despite the full LA conversion. The main product for all catalyst is acetic acid. To evaluate the pure impact of the support over activity and to remove the particle size effect, the succinic acid production was normalized over Ru content and dispersion resulting in different TON for all catalysts (Fig. 6B). Ru/SiO$_2$ and Ru/Zeo stand out among the other catalysts, offering the highest succinic acid production, while the rest present a similar production per mol of Ru. Due to the lack of succinic acid detection for the carbon catalyst, the TON for this catalyst could not be calculated. A clear dependence on the nature of support can be seen pointing out to an important influence of support'

acid sites on succinic acid yield. The most active samples are also the samples with the highest total acidity. The calculated carbon balance (percentage of maintained carbon after the reaction) indicates distinct carbon loss within the series of catalysts. The loss of carbon is assigned to the formation of CO_2 via total oxidation of reagent and products. The higher the conversion values, the lower the carbon balance (Fig. 6B). The unexpectedly low carbon balance of Ru/C catalyst suggest a possible effect of the particle size on the total oxidation activity. If we plot the AA and SA yields against the conversion (Fig. 6C), both decrease with the increase of the conversion, clearer for SA than for AA. Considering this, the catalyst with the smallest crystallite size (Ru/C) presents the highest conversion (100%), the lowest carbon balance (8%) and produces only AA.

The change of the oxidant from O_2 to H_2O_2 results in a very low conversion and yields in both, acetic and succinic acid and suggesting that the active phase is better performing in presence of dissolved oxygen. Low activity of Ru was also observed by Podolean et al. [20] and assigned to the decomposition tendency of hydrogen peroxide over Ru catalysts. Surprisingly the formation of succinic acid is detected for the Ru/C catalyst, which in presence of oxygen results only in acetic acid.

Taking into account the reaction scheme proposed in the literature [4,33] we can imagine that Ru as active site gives priority to the acetic acid route while the use of acid high BET surface supports such as zeolite or SiO$_2$ favors the production of succinic acid in presence of oxygen
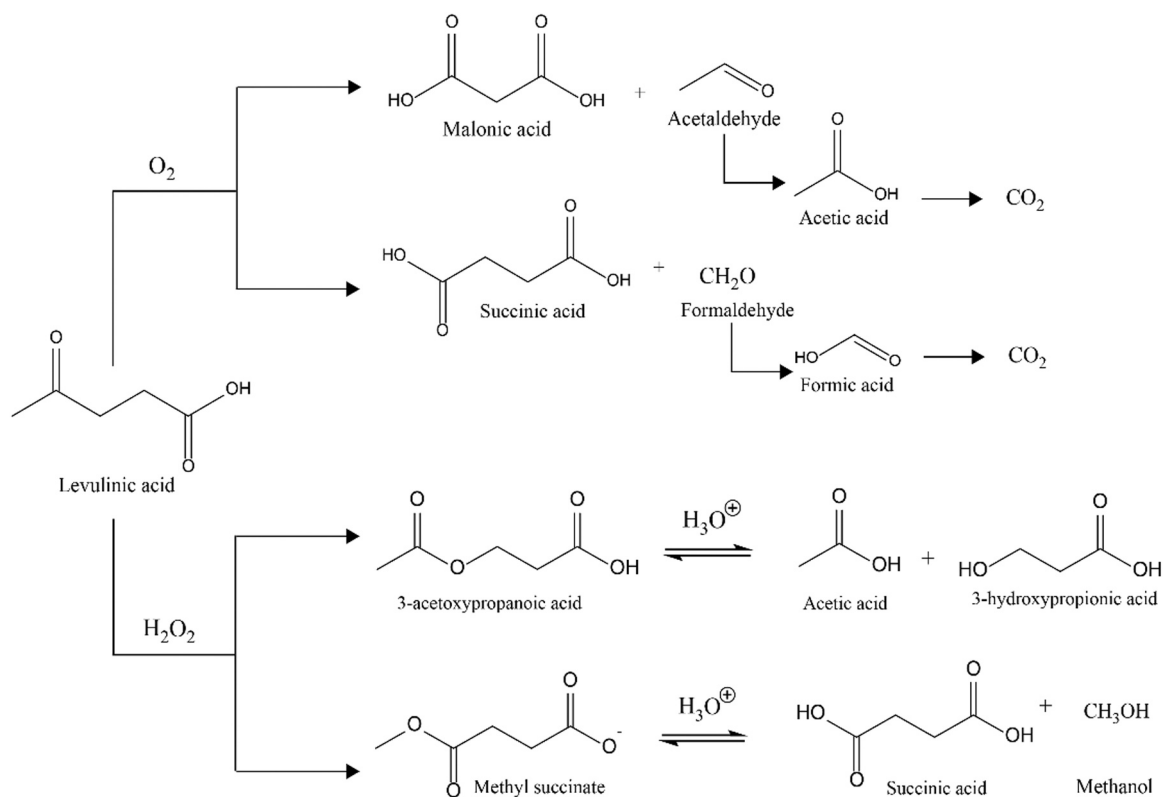
Scheme 1. Proposed routes of LA oxidation to succinic acid and parallel route to acetic acid formation.

(Scheme 1). Whatever the oxidant, stronger oxidizing condition result in levulinic acid conversion to acetic acid [12].

As for the support effect obviously the BET surface area is not the primordial factor as the highest surface support C results in poor succinic acid yield. On the contrary support' nature and acidity matters as the Ru/Zeo and Ru/SiO$_2$ catalysts present the best SA yields.

On the other hand, the metallic particle size appears to be important especially for levulinic acid conversion. Lower the size higher the over-oxidation either to acetic acid or to CO$_2$ and lower the succinic acid yield.

Conclusions

A series of ruthenium catalyst on different supports were prepared with different textural and acidic properties according to the nature of used supports. Well dispersed Ru nanoparticles within the 2–11 nm range were obtained with surface metal distribution depending on specific surface area of the parent support and average particles size.

All catalysts showed activity in liquid phase levulinic acid oxidation, acetic acid being the main product independently to the oxidizing agent. The yield of the desired product, succinic acid, appears to depend on the nature of support, the most acidic support being the most selective. Lowest size particles resulted in higher levulinic acid conversion and much lower succinic acid yield due to over-oxidation of the levulinic to acetic acid. High LA conversion also reflects in lower carbon balance indicating that the catalysts indiscriminately oxidized the products to CO$_2$.

Declaration of Competing Interest

The authors declare that they have no known competing financial interests or personal relationships that could have appeared to influence the work reported in this paper.

Acknowledgments

Appendix A. Supporting information

Supplementary data associated with this article can be found in the online version at doi:10.1016/j.nxmate.2023.100059.

References

[1] Ch Li, Kh. Lun Ong, X. Yang, C. Sze Ki Lin, Bio-refinery of waste streams for green and efficient succinic acid production by engineered *Yarrowia lipolytica* without pH control, Chem. Eng. J. 371 (2019) 804–812, https://doi.org/10.1016/j.cej.2019.04.092.

[2] J.V. Haveren, E.L. Scott, J. Sanders, Bulk chemicals from biomass, Biofuels Bioprod. Biorefin. 2 (2008) 41–57, 10.1002/bbb.

[3] W.M. Budzianowski, High-value low-volume bioproducts coupled to bioenergies with potential to enhance business development of sustainable biorefineries, Renew. Sustain. Energy Rev. 70 (2017) 793–804, https://doi.org/10.1016/j.rser.2016.11.260.

[4] D. Carnevali, M.G. Rigamonti, T. Tabanelli, G.S. Patience, F. Cavani, Levulinic acid upgrade to succinic acid with hydrogen peroxide, Appl. Catal. A Gen. 563 (2018) 98–104, https://doi.org/10.1016/j.apcata.2018.06.034.

[5] C. Antonetti, M. Melloni, D. Licursi, S. Fulignati, E. Ribechini, S. Rivas, J.C. Parajó, F. Cavani, A.M. Raspolli Galletti, Microwave-assisted dehydration of fructose and inulin to HMF catalyzed by niobium and zirconium phosphate catalysts, Appl. Catal. B Environ. 206 (2017) 364–377, https://doi.org/10.1016/j.apcatb.2017.01.056.

[6] A.G. Laurenza, O. Losito, M. Casiello, C. Fusco, A. Nacci, V. Pantone, L. D`Accolti, Valorization of cigarette butts for synthesis of levulinic acid as top value-added chemicals, Sci. Rep. 11 (1) (2021) 1, https://doi.org/10.1038/s41598-021-95361-4.

[7] T. Werpy, G. Petersen, Top Value Added Chemicals from Biomass: Volume I – Results of Screening for Potential Candidates from Sugars and Synthesis Gas, 2004 (DOE/GO-102004-1992, 15008859; p. DOE/GO-102004-1992, 15008859). https://doi.org/10.2172/15008859.

[8] J.J. Bozell, G.R. Petersen, Technology development for the production of biobased products from biorefinery carbohydrates—The US Department of Energy's "Top

10" revisited, Green Chem. 12 (4) (2010) 539–554, https://doi.org/10.1039/B922014C.

[9] A.T. Adeleye, H. Louis, O.U. Akakuru, I. Joseph, O.C. Enudi, D. Michael, A review on the conversion of levulinic acid and its esters to various useful chemicals, AIMS Energy 7 (2) (2019) 165–185, https://doi.org/10.3934/energy.2019.2.165.

[10] Z. Shao, C. Li, X. Di, Z. Xiao, C. Liang, Aqueous-phase hydrogenation of succinic acid to γ-butyrolactone and tetrahydrofuran over Pd/C, Re/C, and Pd–Re/C catalysts, Ind. Eng. Chem. Res. 53 (23) (2014) 9638–9645, https://doi.org/10.1021/ie5006405.

[11] U.G. Hong, H.W. Park, J. Lee, S. Hwang, J. Yi, I.K. Song, Hydrogenation of succinic acid to tetrahydrofuran (THF) over rhenium catalyst supported on H2SO4-treated mesoporous carbon, Appl. Catal. A Gen. 415–416 (2012) 141–148, https://doi.org/10.1016/j.apcata.2011.12.022.

[12] S. Dutta, L. Wu, M. Mascal, Efficient, metal-free production of succinic acid by oxidation of biomass-derived levulinic acid with hydrogen peroxide, Green Chem. 17 (4) (2015) 2335–2338, https://doi.org/10.1039/C5GC00098J.

[13] Hyohak Song, Sang Yup Lee, Production of succinic acid by bacterial fermentation, Enzym. Microb. Technol. 39 (2006) 352–361, https://doi.org/10.1016/j.enzmictec.2005.11.043.

[14] Yujin Cao, Yugang Cao, Xiangzhi Lin, Metabolically engineered Escherichia coli for biotechnological production of four-carbon 1,4-dicarboxylic acids, J. Ind. Microbiol. Biotechnol. 38 (2011) 649–656, https://doi.org/10.1007/s10295-010-0913-4.

[15] Joeri J. Beauprez, Marjan De Mey, Wim K. Soetaert, Microbial succinic acid production: natural versus metabolic engineered producers, Process Biochem. 45 (2010) 1103–1114, https://doi.org/10.1016/j.procbio.2010.03.035.

[16] E. Stylianou, Ch Pateraki, D. Ladakis, M. Cruz-Fernández, M. Latorre-Sánchez, C. Coll, Ap Koutinas, Biotechnol. Biofuels 13 (2020) 72, https://doi.org/10.1186/s13068-020-01708-w.

[17] Est Oreoluwa Jokodola, V. Narisetty, E. Castro, S. Durgapal, F. Coulon, R. Sindhu, P. Binod, J. Rajesh Banu, G. Kumar, V. Kumar, Bioresour. Technol. 344 (Part B) (2022), 126224, https://doi.org/10.1016/j.biortech.2021.126224.

[18] Hemant Choudhary, Shun Nishimura, Kohki Ebitani, Metal-free oxidative synthesis of succinic acid from biomass-derived furan compounds using a solid acid catalyst with hydrogen peroxide, Appl. Catal. A Gen. 458 (2013) 55–62, https://doi.org/10.1016/j.apcata.2013.03.033.

[19] Ryosuke Kawasumi, Shodai Narita, Kazunori Miyamoto, Kenichi Tominaga, Ryo Takita, Masanobu Uchiyama, One-step conversion of levulinic acid to succinic acid using I2/t- BuOK system: the iodoform reaction revisited, Sci. Rep. 7 (2017) 17967, https://doi.org/10.1038/s41598-017-17116-4.

[20] I. Podolean, V. Kuncser, N. Gheorghe, D. Macovei, V.I. Parvulescu, S.M. Coman, Ru-based magnetic nanoparticles (MNP) for succinic acid synthesis from levulinic acid, Green Chem. 15 (11) (2013) 3077–3082, https://doi.org/10.1039/C3GC41120F.

[21] Junxia Liu, Zhongtian Du, Tianliang Lu, Jie Xu, Conversion of levulinate into succinate through catalytic oxidative carbon-carbon bond cleavage with dioxygen, ChemSusChem 6 (2013) 2255–2258, https://doi.org/10.1002/cssc.201300325.

[22] A.P. Dunlop, S. Smith, US Patent 2676186, 1954.

[23] Shanti Kumari Pandey, S.P.S. Yadav, Manju Prasad, Janak Prasad, Mechanism of Ru(III) catalysis in oxidation of levulinic acid by acidic solution of N-bromobenzamide, Asian J. Chem. 11 (1999) 203–206.

[24] Fei Xia, Zhongtian Du, Junxia Liu, Yangyang Ma, Jie Xu, Catalytic oxidative C–C bond cleavage route of levulinic acid and methyl levulinate, RSC Adv. 6 (2016) 72744, https://doi.org/10.1039/c6ra16149a.

[25] Yuran Wang, Ferdinand Vogelgsang, Yuriy Román-Leshkov, Acid-catalyzed oxidation of levulinate derivatives to succinates under mild conditions, ChemCatChem 7 (2015) 916–920, https://doi.org/10.1002/cctc.201403014.

[26] N. Rodríguez, Y.Y. Agámez-Pertuz, E. Romero, J. de J. Díaz-Velásquez, J. A. Odriozola, M.Á. Centeno, Effect of starch as binder in carbon aerogel and carbon xerogel preparation, J. Non-Cryst. Solids 522 (2019) 119554, https://doi.org/10.1016/j.jnoncrysol.2019.119554.

[27] S. Ivanova, V. Pitchon, C. Petit, Application of the direct Exchange method in the preparation of gold catalysts supported on different oxide materials, J. Mol. Catal. A Chem. 256 (2006) 278–283.

[28] S. Loridant, Raman spectroscopy as a powerful tool to characterize ceria-based catalysts, Catal. Today 373 (2021) 98–111, https://doi.org/10.1016/j.cattod.2020.03.044.

[29] A. Porta, L. Falbo, C.G. Visconti, L. Lietti, C. Bassano, P. Deiana, Synthesis of Ru-based catalysts for CO2 methanation and experimental assessment of intraporous transport limitations, Catal. Today 343 (2020) 38–47, https://doi.org/10.1016/j.cattod.2019.01.042.

[30] J.S. Gao, Z.Q. Tian, Surface Raman spectroscopic studies of ruthenium, rhodium and palladium electrodes deposited on glassy carbon substrates, Spectrochim. Acta Part A Mol. Biomol. Spectrosc. 53 (10) (1997) 1595–1600, https://doi.org/10.1016/S1386-1425(96)01855-0.

[31] C. Powell, X-ray Photoelectron Spectroscopy Database XPS,Version 4.1, NIST Standard Reference Database 20 [Data set], National Institute of Standards and Technology, 1989. https://doi.org/10.18434/T4T88K.

[32] D.J. Morgan, Resolving ruthenium: XPS studies of common ruthenium materials, Surf. Interface Anal. 47 (2015) 1072–1079, https://doi.org/10.1002/sia.5852.

[33] A. Chatzidimitriou, J.Q. Bond, Oxidation of levulinic acid for the production of maleic anhydride: Breathing new life into biochemicals, Green Chem. 17 (8) (2015) 4367–4376, https://doi.org/10.1039/C5GC01000D.